International Journal of
Molecular Sciences

MDPI

Article

The Role of Hydrogen Incorporation into Amorphous Carbon Films in the Change of the Secondary Electron Yield

Nenad Bundaleski [1,*], Carolina F. Adame [1], Eduardo Alves [2,3], Nuno P. Barradas [2,3], Maria F. Cerqueira [4,5], Jonas Deuermeier [6], Yorick Delaup [7], Ana M. Ferraria [8,9], Isabel M. M. Ferreira [6], Holger Neupert [7], Marcel Himmerlich [7], Ana Maria M. B. do Rego [8,9], Martino Rimoldi [7], Orlando M. N. D. Teodoro [1], Mikhail Vasilevskiy [4,5] and Pedro Costa Pinto [7,*]

1 Centro de Física e Investigação Tecnologica, Departamento de Física, Faculdade de Ciências e Tecnologia, Universidade Nova de Lisboa, Campus de Caparica, 2829-516 Caparica, Portugal; c.adame@campus.fct.unl.pt (C.F.A.); odt@fct.unl.pt (O.M.N.D.T.)
2 Departamento de Engenharia e Ciências Nucleares, Instituto Superior Técnico, University of Lisbon, 2695-066 Bobadela, Portugal; ealves@ctn.tecnico.ulisboa.pt (E.A.); nunoni@ctn.tecnico.ulisboa.pt (N.P.B.)
3 Instituto de Plasmas e Fusão Nuclear, Instituto Superior Técnico, University of Lisbon, 1049-001 Lisbon, Portugal
4 Centre of Physics of the Universities of Minho and Porto (CF-UM-UP) and Laboratorio de Física para Materiais e Tecnologias Emergentes (LaPMET), 4710-057 Braga, Portugal; fcerqueira@fisica.uminho.pt (M.F.C.); mikhail@fisica.uminho.pt (M.V.)
5 International Iberian Nanotechnology Laboratory (INL), Av. Mestre José Veiga, 4715-330 Braga, Portugal
6 Centro de Investigação de Materias (Lab. Associade I3N), Departamento de Ciência dos Materiais, Faculdade de Ciências e Tecnologia, Universidade Nova de Lisboa, Campus de Caparica, 2829-516 Caparica, Portugal; j.deuermeier@fct.unl.pt (J.D.); imf@fct.unl.pt (I.M.M.F.)
7 European Organization for Nuclear Research, CERN, 1211 Geneva, Switzerland; yorick.maxence.delaup@cern.ch (Y.D.); holger.neupert@cern.ch (H.N.); marcel.himmerlich@cern.ch (M.H.); martino.rimoldi@cern.ch (M.R.)
8 Associate Laboratory i4HB—Institute for Health and Bioeconomy at Instituto Superior Técnico, Universidade de Lisboa, Av. Rovisco Pais, 1049-001 Lisbon, Portugal; ana.ferraria@tecnico.ulisboa.pt (A.M.F.); amrego@ist.utl.pt (A.M.M.B.d.R.)
9 iBB—Institute for Bioengineering and Biosciences and Departamento de Engenharia Química, Instituto Superior Técnico, Universidade de Lisboa, Av. Rovisco Pais, 1049-001 Lisbon, Portugal
* Correspondence: n.bundaleski@fct.unl.pt (N.B.); pedro.costa.pinto@cern.ch (P.C.P.); Tel.: +351-920-552-850 (N.B.); +41-754-114-468 (P.C.P.)

Abstract: Over the last few years, there has been increasing interest in the use of amorphous carbon thin films with low secondary electron yield (SEY) to mitigate electron multipacting in particle accelerators and RF devices. Previous works found that the SEY increases with the amount of incorporated hydrogen and correlates with the Tauc gap. In this work, we analyse films produced by magnetron sputtering with different contents of hydrogen and deuterium incorporated via the target poisoning and sputtering of C_xD_y molecules. XPS was implemented to estimate the phase composition of the films. The maximal SEY was found to decrease linearly with the fraction of the graphitic phase in the films. These results are supported by Raman scattering and UPS measurements. The graphitic phase decreases almost linearly for hydrogen and deuterium concentrations between 12% and 46% (at.), but abruptly decreases when the concentration reaches 53%. This vanishing of the graphitic phase is accompanied by a strong increase of SEY and the Tauc gap. These results suggest that the SEY is not dictated directly by the concentration of H/D, but by the fraction of the graphitic phase in the film. The results are supported by an original model used to calculate the SEY of films consisting of a mixture of graphitic and polymeric phases.

Keywords: amorphous carbon; particle accelerators; SEY; XPS; Raman spectroscopy

check for updates

Citation: Bundaleski, N.; Adame, C.F.; Alves, E.; Barradas, N.P.; Cerqueira, M.F.; Deuermeier, J.; Delaup, Y.; Ferraria, A.M.; Ferreira, I.M.M.; Neupert, H.; et al. The Role of Hydrogen Incorporation into Amorphous Carbon Films in the Change of the Secondary Electron Yield. *Int. J. Mol. Sci.* **2023**, *24*, 12999. https://doi.org/10.3390/ijms241612999

Academic Editor: Christian M. Julien

Received: 17 July 2023
Revised: 10 August 2023
Accepted: 18 August 2023
Published: 20 August 2023

1. Introduction

The emission of secondary electrons from surfaces plays a key role in the generation of electron multipacting in high-power radio frequency devices and particle accelerators with positively charged beams. In particle accelerators, it can result in the formation of clouds of electrons, causing beam instabilities, deterioration of the vacuum, or heat loads to cryogenics parts of the system, limiting the overall efficiency of the accelerator (i.e., the beam luminosity) [1–6]. A possible cure to this problem is to reduce the electron emission by coating the internal surfaces of the vacuum chambers with a thin film of low Secondary Electron Yield (SEY) material. Amorphous carbon (a-C) coatings have been successfully used in the Super Proton Synchrotron at CERN (European Organisation for Nuclear Research) to mitigate the electron multipacting [7], and it is now in the baseline for the High Luminosity upgrade of the Large Hadron Collider, (CERN, Geneva, Switzerland) and the Electron Ion Collider, (Brookhaven National Laboratory, Upton, USA) [8,9].

Secondary electron emission can be conveniently described as follows [10]. Primary electrons that penetrate a material mainly lose their energy through different types of electron excitations (via plasmon excitations or by a direct energy transfer to valence and core electrons). This results in the generation of secondary electrons inside the material, with energy above the vacuum level. On their way out, these internal secondary electrons can efficiently lose their energy only through the excitation of valence electrons. Finally, once they reach the surface, only the internal secondary electrons which still have energy above the vacuum level have a chance of being emitted. The whole process is strongly affected by the electronic structure of the material, which determines the energy loss processes of both primary and internal secondary electrons. Particularly important is the latter, which can be reduced by opening the energy gap. This is the origin of the high SEY of dielectric materials [11].

The efficiency of a-C coatings for suppressing electron multipacting depends on the structural properties: only coatings with pronounced electrical conductivity can have a low SEY. It has been well-established that the presence of hydrogen impurities is particularly harmful in that respect [12,13]. The effects of hydrogen and nitrogen impurities on the secondary electron emission properties of a-C coatings were the subject of two recent studies [14,15]. It was clearly demonstrated that adding hydrogen or deuterium in the discharge gas increases the SEY of carbon films, while the presence of nitrogen allows for the opposite, which can be used to compensate the effect of hydrogen. By combining SEY measurements with Ion Beam Analysis (IBA), a correlation between the deuterium content and the maximum SEY (SEY_{max}) was established. The SEY_{max} increases linearly, from 1 to 1.4, when the overall hydrogen and deuterium (H + D) relative content increases up to 47%. A further increase of the H + D amount up to 54% is accompanied by a steep SEY_{max} growth to 2.2. The samples were also investigated using Optical Absorption Spectroscopy (OAS), enabling the estimation of the optical energy gap using the procedure established by Tauc (the so-called Tauc gap). These results reveal a strong correlation between the SEY_{max} and the Tauc gap, apparently offering a straightforward explanation for the SEY_{max} increase. However, a-C films are often non-uniform, i.e., they may consist of various regions with different compositions and electronic structures (e.g., graphitic, diamond-like, and hydrocarbon domains—the latter being a result of highly common hydrogen contamination) [16]. Such materials have different local energy gaps, limiting the interpretation of Tauc plots [17].

Robertson summarised the measurements of the Tauc gap performed on different types of a–C (pure and hydrogenated) in his seminal review paper [18]. He concluded that the Tauc gap of a film is not determined by the hydrogen content, but by the relative amount and properties of the sp^2 carbon phase. The local energy gaps of diamond-like and various hydrocarbon phases are too large to be related with a Tauc gap below ≈ 2 eV. The gap is therefore related to the configuration of π states on the sp^2 sites. In a planar cluster model, the band gap of a given cluster is inversely proportional to the square root of the number of the hexagonal rings in the cluster [16]. Different types of defects (e.g., formation

of pentagons or heptagons) will also open the gap. From this perspective, deviation from the linear dependence at low photon energies in Tauc plots should not be attributed to the so-called tail states (i.e., Urbach tail), but to the small quantity of graphitic clusters with small local energy gaps.

The abrupt increase of the SEY_{max}, when the H + D relative concentration changes from 47% to 54%, suggests that the hydrogen content may not be directly responsible for the change in the secondary electron emission (SEE) properties of a-C films. This doubt is further supported by the high correlation between the SEY_{max} and the Tauc gap [14,15], with the knowledge that the Tauc gap can be independent of the hydrogen concentration [18]. This aspect motivates our study: as the Tauc gap in a-C is known to be affected by the concentration and size of the graphitic domains, could the latter also influence the SEE?

In our recent work, we performed the deposition of a-C coatings using magnetron sputtering in Ar discharges with several fractions of D_2 and identified the mechanism behind the incorporation of deuterium in the films during the production phase and its impact on the SEY [15]. It is expected that the incorporation of deuterium affects the electronic structure of a–C, and therefore its SEY, in practically the same way as hydrogen impurities would. At the same time, adding deuterium allows these intentionally added species to be distinguished from the natural hydrogen contamination that originates from the residual background of H containing molecules in the coating system during film deposition, as well as from the surface contamination that mainly derives from hydrocarbons after removal from the vacuum system. In this work, we provide detailed analysis of the same samples by means of different electron and vibrational spectroscopic techniques. X-ray and UV Photoelectron Spectroscopies (XPS and UPS, respectively) were used to determine the surface composition, to identify different phases in the a-C films, and to obtain information on their electronic structure. Further insights are provided using Raman scattering, Fourier Transform Infrared Spectroscopy (FTIR), and High-Resolution Electron Energy Loss Spectroscopy (HREELS). The Raman scattering characterisation, which enabled the detection of the presence of graphitic carbon, was particularly valuable in supporting the interpretation of the XPS results. FTIR and HREELS were used to identify the character of the C–D bonds in the most contaminated samples. These results are then compared with the corresponding SEY, OAS, and IBA measurements, enabling us to reveal the actual mechanism behind the SEY increase caused by the hydrogen contamination.

2. Results

2.1. Composition, Electron Emission and Optical Properties of the Coatings

In this section, we summarise the main results of the thin films obtained using different techniques and reported in [15]. Thin film composition analysis, performed by IBA, revealed the presence of uniformly distributed C, D, H, and O through the whole film depth, as confirmed by the Secondary Ion Mass Spectrometry measurements. The results of the quantitative composition, the mass densities of the films—estimated from the IBA measurements—and the film thicknesses (obtained by Scanning Electron Microscopy), as well as the results of the SEY and Tauc gap (E_T) measurements, are summarised in Table 1. The amount of incorporated deuterium steadily increases for an increasing D_2 partial pressure in the discharge gas (p_{D2}), getting relatively close to the theoretical maximum of 65 at.% in saturated hydrocarbons. The dependence of the maximum secondary electron yield (SEY_{max}) on p_{D2} in the films has a different trend: an increase of the H/D amount from 10 to 46 at.% changes SEY_{max} from 0.99 to 1.38, while additional 7 at.% of H/D increases the SEY_{max} abruptly to 2.2. Furthermore, the SEY_{max} and the Tauc gap are strongly correlated. It appears that small changes of the D/H content in samples 1D and 10D are accompanied by very different electronic structures, which govern both the secondary electron emission and optical properties. The latter is also clear from the fact that the sample 1D was conductive, in contrast to the sample 10D, which appeared to be

insulating. This aspect required the measurement of the SEY of this charging sample in a different experimental setup, using a pulsed electron beam [15].

Table 1. Variation of the composition (in at.%), SEY_{max} and the Tauc gap and mass density of a-C films deposited by intentionally adding different amounts of D_2 in the discharge gas [15].

Sample	p_{D2} (Pa)	C (%)	H (%)	D (%)	O (%)	SEY_{max}	E_T (eV)	ρ (g/cm^3)
Reference	0	83.4	11.7	0	4.9	0.99	0.12	1.44
0.2D	3.8×10^{-3}	77.9	9.8	9.6	2.7	1.03	0.37	1.99
0.5D	1.1×10^{-2}	67.8	6.0	23.7	2.5	1.15	0.78	1.91
1D	2.6×10^{-2}	52.2	6.3	39.9	1.6	1.38	1.17	2.34
10D	2.2×10^{-1}	45.2	2.8	50.4	1.6	2.03	2.29	1.15

Based on the mass densities and the Tauc gaps of the films, we can already make a first estimation of their structure using the general guidelines summarised in [19] and by considering that deuterated carbon films are generally somewhat denser than their hydrogenated equivalent. It appears that the reference sample, as well as the 0.2D and 0.5D samples, with their Tauc gaps being clearly below 1 eV, are most likely dominated by graphitic and partially deuterated graphite-like (a-C:D) regions. The 1D sample, which exhibits a high density, a large H + D content leading to E_T = 1.38 eV, high density, and a large H + D content, might be closest to diamond-like a-C:D. Finally, the 10D sample, characterised by a low density and E_T > 2 eV, could be a typical example of a polymer-like a–C:D.

2.2. XPS Measurements

Apart from carbon, the survey XPS spectra of all the samples show the presence of ~8 at.% of oxygen at the surface. The samples were not charging during the measurements, except for the sample 10D, which was therefore measured utilising an electron flood gun for charge compensation. The O 1s line in the first four samples was situated at 532.6 eV. Assuming that the O 1s line position is the same in the sample 10D, the latter was used as a binding energy reference for that sample, and all the spectra were shifted accordingly.

Hydrogenated/deuterated a-C is expected to be a mixture of graphitic (pure sp^2 hybridised) carbon, diamond-like carbon and different hydrocarbons, in which carbon could be in both sp^2 and sp^3 hybridisation. Resolving these distributions in the C 1s photoelectron line is a complex problem due to their quite small chemical peak shifts, as extensively discussed in the literature [20–23]. The graphitic contribution is located at 284.3–284.5 eV, while a pure sp^3 C contribution is usually encountered at about 285.2 eV [21]. The latter feature overlaps with different hydrocarbon contributions, around 285.0 eV, while at higher binding energies, further contributions related to various carbon bonds with O can be expected [23,24]. All peaks should be symmetric apart the one from the pure graphitic contribution, which is highly asymmetric [22,23]. The peak model for the graphitic contribution could be established by measuring the C 1s photoelectron line of a freshly cleaved Highly Oriented Pyrolytic Graphite (HOPG) crystal. Unfortunately, the asymmetry of the graphitic contribution becomes less pronounced with the cluster size reduction and with the increase in the amount of defects in this phase. These factors make bond identification through fitting the C 1s line spectrum a challenging task, without a straightforward solution. However, the elemental O concentration can be used as an additional constraint, which the carbon-oxygen bond contributions in the C 1s line need to follow. This approach, applied to all the samples except 10D (see below), strengthens the reliability of the interpretation of the spectra taken from the a-C coatings.

The high-resolution spectra of the C 1s photoelectron line of a freshly cleaved HOPG and the five samples considered in this study, together with the corresponding fittings, are presented in Figure 1. In all cases the background was calculated using the Shirley algorithm. As in [14], we again observe that the C 1s line becomes more symmetric with the increase of the D content in the films. One possible explanation of this trend is that the

relative amount of graphitic C is reduced and/or that the clusters become smaller with the increase of the D content.

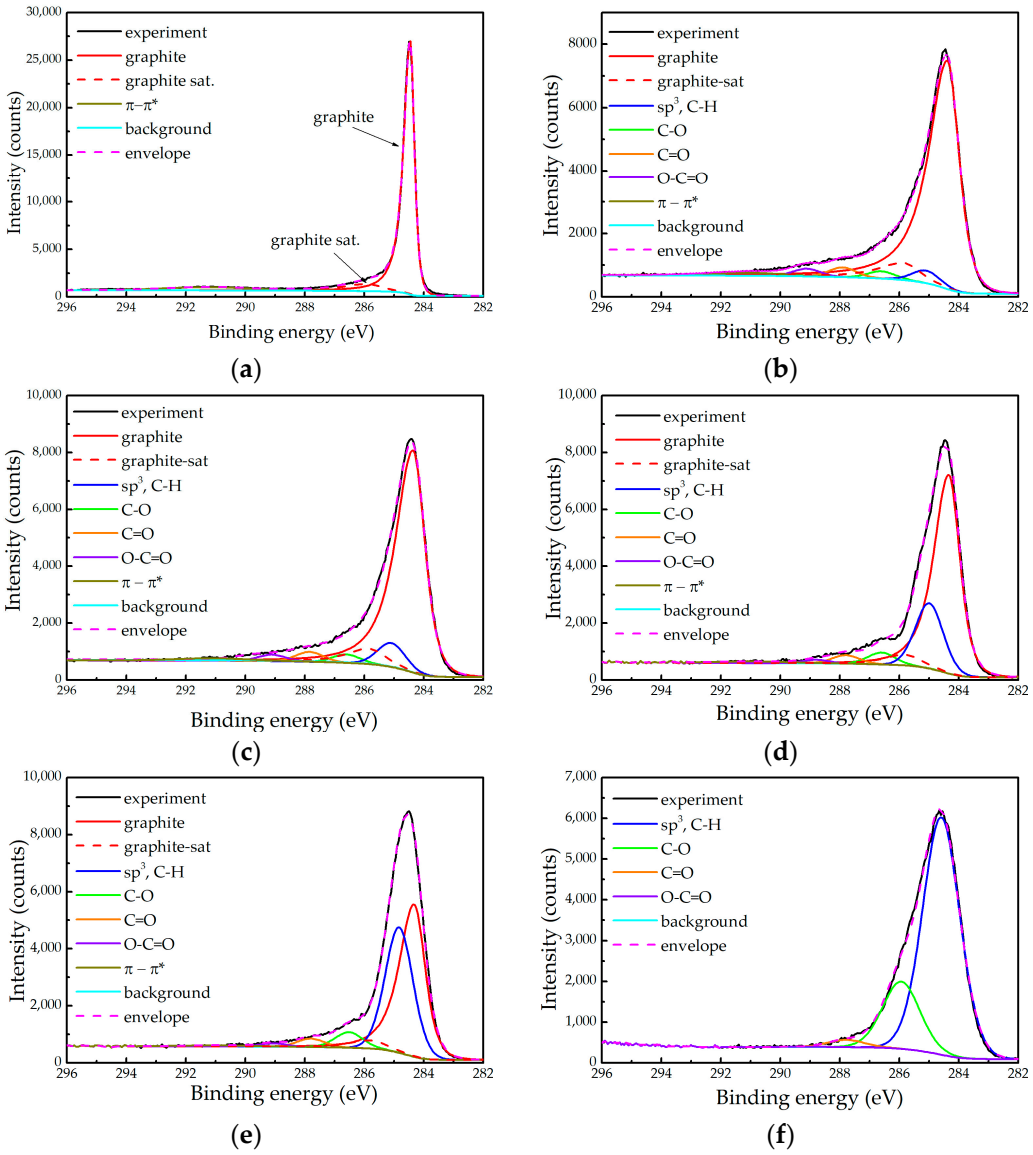

Figure 1. High resolution spectra of the C 1s state of (**a**) freshly cleaved HOPG; (**b**) reference a-C sample; (**c**) sample 0.2D; (**d**) sample 0.5D; (**e**) sample 1D; and (**f**) sample 10D, including the peaks obtained through data fitting, as described in the text.

The C 1s spectrum of HOPG (Figure 1a) was fitted using three contributions. The main peak (graphite) at 284.45 eV has an asymmetric profile with a nomenclature LA(1.2, 2.5, 5) in the CasaXPS software [25] and a full width at half maximum (FWHM) of 0.34 eV. It should be stressed that the same peak profile was used by M. Biesinger, and failed to secure perfect agreement with the measured spectrum [23]. As a similar problem appeared in our spectra, we introduced a second peak ("graphite sat"), with the same profile and a FWHM of 1.3 eV. This peak is shifted with respect to the first towards higher binding energy by 1.47 eV, while their intensity ratio is 0.106. Finally, there is a well-known wide symmetric peak at about 291.2 eV attributed to the π-π^* satellite always present in spectra of pure graphite [22,23].

It might be tempting to interpret the peak "graphite sat" as evidence of defects, such as sp^3 carbon or C-H bonds. However, one should bear in mind that such contributions would be symmetric. The asymmetry of this contribution would then imply the non-negligible

presence of other contaminants (typically O). that XPS is distinctively more sensitive to such contaminants than to C [26], the corresponding photoelectron lines would be clearly observable. Since this is not the case, we assume that both contributions originate from perfect graphite. They are introduced to better describe the shape of the C 1s line of HOPG, without attributing any physical interpretation to this separation. In our fittings of the graphitic contribution, we fixed the relative positions of the first two peaks and kept their intensity ratio approximately constant (see below). The intensity of the third peak was considered to be a free parameter (the latter is affected by the electronic structure and size of the graphitic clusters). The profile of all the symmetric peaks (attributed to less conductive phases in a-C films) was of pseudo-Voigt type GL(30). They are attributed to sp^3 carbon and C-H(D) bonds with both sp^2 and sp^3 carbon (284.8–285.2 eV), C-O (≈286.6 eV), C=O (287.8–288.2 eV), and O-C=O (≈289.0 eV) bonds [21,24]. All symmetric peaks within one spectrum have FWHMs fixed to the same value.

The essential element of the fitting procedure was to maintain the intensities of the peaks attributed to the carbon-oxygen bonds in the C 1s line in accordance with the O:C concentration ratio obtained from the quantitative analysis, being 8 ± 0.8% for all samples. In this approach, we consider that the C:O stoichiometric ratio is 1:1 for the C-O and C=O contributions and 2:1 for the COO contribution. Consistency between the composition and the C 1s fits could only be achieved by successively decreasing the asymmetry of the graphitic line as the H + D amount increases. The degree of asymmetry is characterised here by the ratio of the parameters α and β of the line shape LA(α,β,m), which determine the spread of the tail on the high and low binding energy side, respectively (α/β being below 1 for asymmetric line shapes). In addition, final asymmetry tuning of the graphitic contribution was performed through a slight modification of the intensity ratio between the main peak and the "graphite sat" in the range 0.078–0.106. This peak fitting model successfully describes the spectra of almost all of the samples; however, it did not provide consistent results for the sample 10D, as can be seen in Table 2, in which the XPS fitting results are summarised. For this sample, the oxygen content is overestimated, most likely due to the charging problems that affected the shape of the C 1s line.

Table 2. Summary of the relative amounts of different carbon bonds based on the C 1s line fittings in comparison with the relative H + D contents [15].

Sample	α/β	Graphitic (%)	sp^3 C-H (%)	C-O (%)	C=O (%)	-(C=O)-O- (%)	H + D Content (%)
Reference	0.45	88.14	3.29	1.91	2.55	2.01	11.7
0.2D	0.50	85.17	6.43	2.41	2.57	1.73	19.4
0.5D	0.58	71.09	20.4	3.75	2.46	1.05	29.7
1D	0.58	52.75	38.11	4.83	2.46	0.96	46.2
10D	1.00	0	75.99	21.53	2.35	0.13	53.2

The fitting results of the C 1s line taken from the five samples and the relative content of hydrogen and deuterium taken from Table 1 are summarised in Table 2. The following general trends with the increase of the H + D relative content appear:

- The relative contribution of the graphitic component decreases and even disappears in the sample 10D;
- The relative contribution attributed to the sp^3 carbon and the hydrocarbons increases;
- The asymmetry of the graphitic component becomes less pronounced.

Therefore, increasing the amount of incorporated H/D in the films is accompanied by a higher content of hydrocarbons and a reduction in the graphitic content. Besides, the graphitic regions become smaller and/or with higher defect concentration.

At this point, the total disappearance of the graphitic content in the sample 10D is not certain. We can only claim that there is no need to introduce the asymmetric graphitic component to obtain a good fit of the spectrum presented in Figure 1f. As the sample 10D was charging, one could expect a deformation of the line shape. Moreover, the latter

certainly took place as it was not possible to perform a good fit that would justify the correct content of oxygen. While one cannot reliably exclude the presence of some graphitic regions in that sample, their relative amount most likely does not exceed ≈ 10%.

2.3. UPS Measurements

In Figure 2, we present UPS spectra close to the Fermi level (binding energy of 0 eV) of freshly cleaved HOPG, the reference sample without D, as well as of the samples 0.2D, 0.5D and 1D. The spectra are normalised with respect to their intensities at 2 eV. The same structure cannot be reliably measured for the sample 10D due to the charging problems.

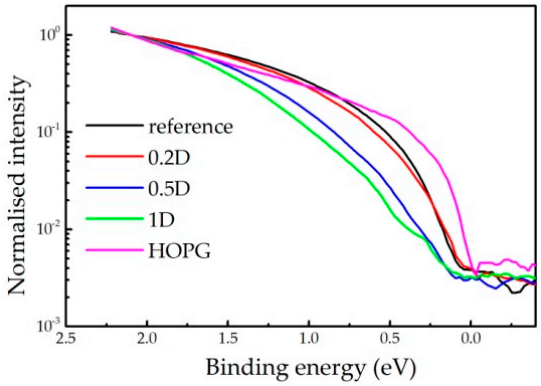

Figure 2. Valence bands electron spectra excited by He I radiation of HOPG and a-C coatings with different D content. The data are normalised at binding energy of 2 eV.

The very top of the valence band of the HOPG (binding energy range 0–1 eV) is attributed to π electrons from the K point of the Brillouin zone [27]. As the diamond-like and hydrocarbon regions have energy gaps well above 2 eV [18], the presence of the signal in other samples is additional evidence of the existence of graphitic regions in the a–C samples. The intensity of this structure gradually decreases with the increasing H + D content, as previously concluded from the XPS spectra. A closer inspection of the spectra reveals that the top of the valence band shifts towards a higher binding energy as the H + D content increases. This verifies an opening of the local energy gap, which implies a size reduction of the graphitic regions [16,28] in the films.

The difference between the top of the valence band and the Fermi level (the latter corresponds to the 0 eV binding energy) in the spectra presented in Figure 2 is in the 0.0–0.2 eV range. Assuming that the Fermi level is around the mid-gap position, the energy gap of the graphitic regions can be roughly estimated to be ≈0.2 eV for the reference sample and the 0.2D sample, and ≈0.4 eV for the samples 0.5D and 1D. In a first approximation, the UPS value for the reference sample corresponds to its Tauc gap (Table 1), while the mismatches between the UPS and Tauc values for the other samples (particularly for 1D) are much higher. The latter is due to the character of the Tauc gap, which corresponds to the electronic properties of the dominant components in the film, whereas the UPS detects the highest occupied states. Therefore, reasonable agreement between the Tauc gap measurements and the UPS results of the reference and 0.2D samples is additional evidence of their graphitic character. On the other hand, the mismatch in the case of the other two samples confirms a lower graphitic content, as already revealed by the XPS results.

2.4. Raman Spectroscopy

Further insight into the structure of the thin films was obtained using Raman scattering spectroscopy. The results of the Raman spectroscopy performed on the samples deposited on silicon using the 532 nm laser beam are summarised in Figure 3. The representative spectra of most of the samples (excluding the sample 10D) are presented in Figure 3a. The steady increase of the Raman signal with the increasing D_2 content in the discharge gas is most likely due to a drop of the optical absorption [15], which is also manifested in the

increase of the Tauc gap (cf. Table 1), combined with the monotonic increase of the film thickness with the H + D content.

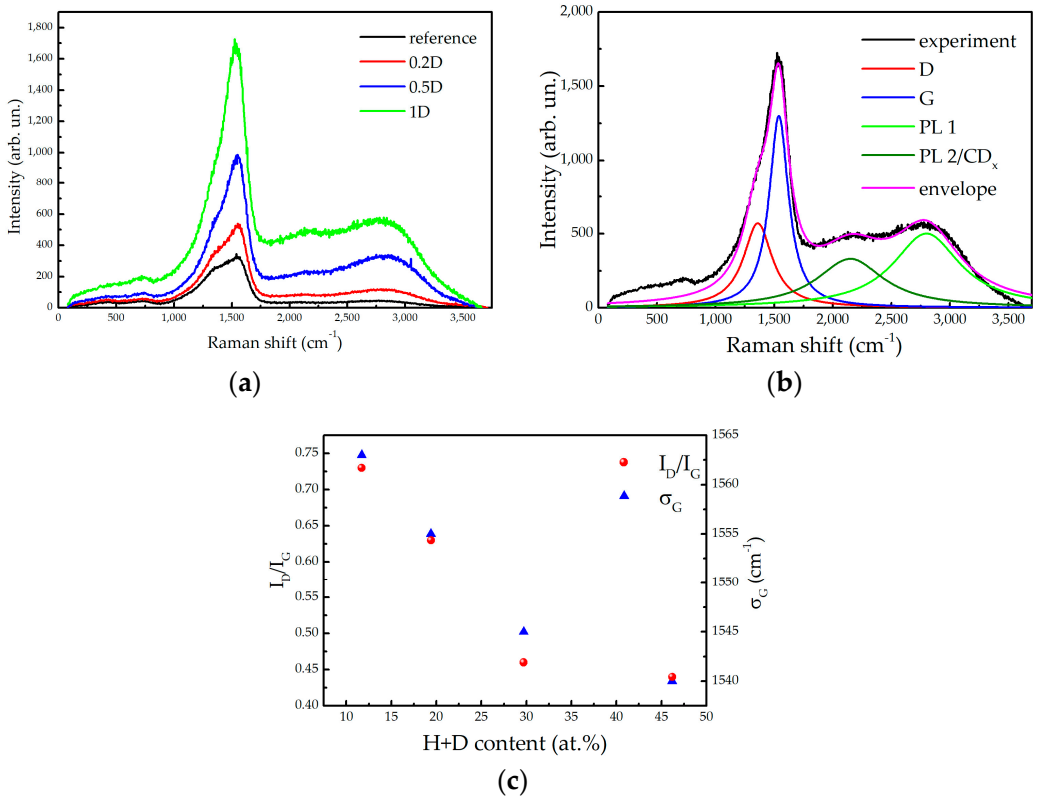

Figure 3. (**a**) Raman spectra of the reference sample, as well as of the 0.2D, 0.5D and 1D films deposited on Si substrates measured using a 0.7 W laser beam of 532 nm wavelength; (**b**) Fitting illustration on the example of the sample 1D; (**c**) intensity ratio of the D and G bands I_D/I_G and position of the G band maximum σ_D vs. the relative H + D film content.

The feature in the 1100–1700 cm^{-1} range corresponds to the overlapping G and D bands, being typical for various carbon phases [29] (including deuterated a–C films [30]). The G band is attributed to sp^2 carbon atoms (it is not restricted to sixfold carbon rings in graphite nor to pure carbon phases). The D band is a fingerprint of isolated sixfold carbon aromatic rings, being forbidden in a perfect graphite [16]. The co-existence of both bands therefore implies the presence of graphitic regions that are separated by disordered phases.

In addition to the G and D bands, an intense wide structure at about 2800 cm^{-1} can be also observed in Figure 3a. Its intensity relative to the G and D bands increases with the amount of deuterium incorporated in the samples. In the sample 10D, the intensity of this structure is about 10 times greater than in the other samples when measured using the same experimental conditions, thus hindering an identification of the graphitic carbon in this case (more details on this matter are provided in Supplementary Information S1). Raman spectra of carbon-based materials may have some bands in this range. For instance, graphene is characterised by the 2D mode at around 2700 cm^{-1} and a second order D + D′ band at around 2900 cm^{-1} [31]; Raman spectra of polymeric amorphous carbon exhibit a C-H stretching band in this range [29,32]. To clarify the origin of this band, Raman measurements were also performed using a He-Ne laser (wavelength 632.8 nm), resulting in a lack of this structure (cf. Supplementary information S1). The absolute energy position of this feature is ≈1.97 eV, corresponding well to the position of the broad emission band (1.9–2.5 eV) observed in a photoluminescence of hydrogenated a–C [33]. Therefore, we conclude that this feature is not a Raman signal, but is evidence of photoluminescence—it is related to the excitation of electronic states. The latter also explains why this feature increases with the increasing deuterium content.

The fitting of the Raman spectra is demonstrated in Figure 3b on the example of the sample 1D, while the other fitting details can be found in Supplementary Information S1. The spectra were fitted using four Lorentzian peaks after removing a linear background. Although this approach did not provide a perfect agreement outside the range of interest (the latter being 1100–3000 cm^{-1}), it allows the extraction of the most valuable information characterising the a-C samples. Two of the Lorentzians are attributed to the G and D bands at about 1550 cm^{-1} and 1360 cm^{-1}, respectively. The peak widths and the position of the D band do not change significantly among the studied samples. There is, however, a substantial difference between the relative peak intensities from the different samples, as well as a clear shift of the G band. The wide hump related to the photoluminescence (PL), was fitted using two contributions, at about 2800 and 2150 cm^{-1}. The latter could also be, at least partially, attributed to the CD_x stretching band [29] (PL2/C-D); the measurements performed at the 632.8 nm excitation support this interpretation (cf. Supplementary Information S1).

Most of the findings concerning the different a–C systems extracted from the Raman spectra are related to the G and D bands. These bands have a large width (≈200 cm^{-1}) in all of the samples, being a characteristic of disordered systems [34]. The ratio of the intensities of the D and G bands, I_D/I_G, and the position of the G band are plotted as a function of the relative H + D content in Figure 3c. The increase of the H + D content in the films reduces the ID/IG intensity ratio from 0.75 to 0.45 (a similar trend has been reported in [35] due to the increase of the hydrogen content), while the G band position σ_D shifts from 1563 to 1540 cm^{-1}. While the observed trends are ambiguous when considered separately, a unique interpretation of this joint information is that the increase of the deuterium content corresponds to stage two of the well-known amorphisation trajectory of graphite, as proposed by Ferrari and Robertson [16]: the transformation of nano-graphite into amorphous carbon. In this amorphisation stage, the I_D/I_G ratio is directly proportional to the average number of carbon atoms in the graphitic clusters, i.e., to the square root of their diameter.

The fitting approach shown in Figure 3b was not applicable to the sample 10D due to the intense curvilinear background, mostly caused by the photoluminescence signal, which makes the extraction of information in the range of the D and G bands unreliable. Nevertheless, such an attempt has been made by removing the background of a polynomial form, which resulted in an asymmetric structure that could be mainly interpreted as the G band, while the D band is apparently lacking. Although of limited reliability, this result implies that the graphitic phase in the sample 10D is extremely small or even absent (see above). Details concerning the analysis of the Raman spectra of the sample 10D can be found in Supplementary Information S1.

In addition, an attempt was made to identify the character of the C-D and C-H bonds using other vibrational spectroscopies, namely FTIR and HREELS. These results are presented in Supplementary Material S2 and Appendix A, respectively. In the case of the FTIR, the signal attributed to C-D bonds was identified only in the case of the sample 10D, revealing that about 60% of the deuterium atoms are bonded to sp^2 carbon. A similar conclusion was obtained from the measurement of the sample 1D through HREELS, which confirmed that the character of the C-D bonds, being practically the same, is not responsible for the large difference between the electronic structures of the two samples. At the same time, the majority of the hydrogen at the surface of the sample 1D is bonded with sp^3 carbon, clearly indicating that it corresponds to surface contamination caused by saturated hydrocarbons.

3. Discussion

The XPS results and the mismatch between the Tauc plot measurements and UPS spectra evidence that the samples are generally non-uniform. Hence, the films should be considered as mixtures of different carbon phases (being a frequent situation [16]), each characterised by their own local energy gaps. The steady increase of the films' density with

the increasing amount of incorporated deuterium up to the sample 1D can be understood as an augmentation of the amount of sp^3 phases that are present in the film (cf. Table 1). At the same time, the sample 10D has the lowest density; despite the similar relative composition compared to the sample 1D, this aspect clearly indicates the formation of a polymeric phase [19]. These estimations are fully supported by the results of the XPS, UPS and Raman analyses, revealing that an increase of the deuterium content is accompanied by a decrease of the overall relative amount of the graphitic regions and their size reduction (i.e., transition from nanocrystalline graphitic phase into amorphous carbon). This is particularly evident when comparing the samples 1D and 10D, which are characterised by similar relative contents of deuterium (Table 1) and practically the same character of C-D bonds. The abrupt increase of the SEY and the Tauc gap from the sample 1D to the sample 10D can be only explained by the dramatic diminishing of the graphitic component (Table 1).

A similar conclusion was obtained by Robertson [18], who demonstrated a nearly linear dependence of the Tauc gap with the sp^2 fraction c_{sp2} for its relative contents below 80%, indicating that the relative hydrogen content does not have a direct influence on the variation of the band gap. As the data presented in [18] are compiled from the works of different authors and measured on various a–C and a–C:H samples, the points are rather scattered. Nevertheless, the line $E_T = 3–2.5 \cdot c_{sp2}$ represents well the observed trend with the Tauc gap uncertainty bar of about $\Delta E_T = \pm 0.25$ eV [36]. The dependences of the Tauc gap and the SEY_{max} on the graphitic content obtained from the XPS analysis of our samples are shown in Figure 4. Both the E_T and SEY_{max} decrease when the relative amount of graphitic regions increases. Moreover, the trend of the Tauc plot fits well with that of Robertson—represented by a dashed blue line—for graphitic contents below 70%. The systematic shift between the two trends, which is within the uncertainty ΔE_T, can be explained by the difference in the ways the graphitic content was determined [36] (using electron energy loss spectroscopy and nuclear magnetic resonance). In addition, at $c_{sp2} > 70\%$, we observe a faster drop of E_T, as expected concerning the non-existent band gap of graphite. These agreements imply that the methodology used to extract the graphitic fraction from the XPS spectra is quite reliable and can also be used to correlate the SEY with the graphitic content.

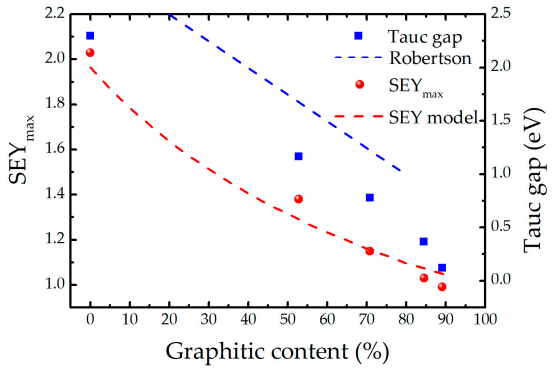

Figure 4. Dependence of the Tauc gap and the SEYmax on the graphitic content in a-C films. The dashed blue line represents the linear dependence of the Tauc gap as reported by Robertson [37]. The dashed red line is the prediction of the modified semi-empirical model for the SEY developed in this work.

The decrease of the SEY with the increase of the graphitic content (observed in Figure 4) is in accordance with the expectations: the higher the fraction of the sp^2 phase, the lower the SEY. A simple model, based on the same assumptions as those used to derive the well-known semi-empirical equation for the SEY [37], was developed to support the observed experimental dependence. This equation, originally derived for uniform samples, was recently modified to encompass multilayer systems [38]. The latter approach was used as a starting point to model non-uniform a-C films as mixtures of two different phases:

a graphitic one and a polymeric one. Therefore, the polymeric phase is considered to be representative of all non-graphitic phases in the films.

In the frame of the semi-empirical theory, the number of internal secondary electrons generated in a depth range of (z, $z + dz$) is equal to $S(z)\cdot dz/\varepsilon(z)$, where S and ε represent the stopping power of the primary electrons and the effective energy required to create one internal secondary electron, respectively. The secondary electrons created at depth z will then be emitted with a probability equal to $0.5\cdot\exp(-z/\lambda)$ [39], where λ is the mean escape depth of secondary electrons, which was taken from the literature [11]. As S, λ and ε are material dependent, they will be changing from point to point of the sample interior.

The first step is to determine the parameters that characterise the electron emission properties of the graphitic and polymeric regions. For this purpose, the SEY dependencies on the primary electron energy of the reference sample and the sample 10D [15] were used as representatives of pure graphitic and pure polymeric material, respectively. Then, for a defined relative graphitic content, it is possible to estimate the range of primary electrons R. The samples were then modelled as a multilayer system with a predefined graphitic content. However, the depth distribution of the different phases within each sample is unknown. Another difficulty in establishing this distribution is in the lateral non-uniformity of the samples. To overcome this problem, a set of M depth distributions were generated (here designated as configurations), each containing the same amount of graphitic carbon, using a Monte Carlo approach. Finally, the $SEY(E)$ was calculated for each configuration by generating $S(E,z)\cdot dz/\varepsilon(z)$ electrons at all depths z in the range [0, R], and calculating their escape probabilities affected by the multilayer structure in the depth interval [0, z]. The whole procedure is described in more detail in Appendix B.

The results of the SEY model, obtained using M = 1000 configurations and for the primary electron energies in the range 50–1000 eV are presented in Figure 4. Bearing in mind the simplifications introduced in the frame of the model, and that the calculated SEY curves were obtained without any adjustments to the existing experimental data, the agreement with the measured values is very good. There is also a built-in systematic error in the model due to the consideration that the reference sample would be purely graphitic, while its actual graphitic content is only 90%. This approximation is responsible for an overestimation of the SEY for the highest graphitic contents. Although the effective energy ε is indeed smaller in the polymeric (40.8 eV) than in the graphitic (60.4 eV) regions, the major difference between the characteristics of the two regions is the mean escape depth λ, being more than two times smaller in graphite (4.9 nm) than in polymers (11 nm). That is probably the reason the SEY_{max} dependence on the sp^2 content has a form of an exponential decay function.

In a sample with a sufficiently high content of the graphitic phase, the regions with a large energy gap (e.g., diamond-like or hydrocarbon regions) will not contribute to the Tauc gap: photons that may penetrate large energy gap regions will most likely be absorbed once they enter a sufficiently large graphitic region. The reduction of the amount and size of the graphitic phase increases the optical transparency of the films and, consequently, the Tauc gap. A similar effect takes place during the transit of secondary electrons through the films. The escape depth of internal secondary electrons, which is directly related to their energy loss mechanisms, is strongly affected by the electronic structure of a material. The efficient energy loss is secured by sufficiently long trajectories of the secondary electrons through graphitic regions characterised by a very narrow energy gap. As in the case of light transmission, the graphitic phase serves as an energy absorber. Once they reach the surface, the secondary electrons will not have enough energy to overcome the energy barrier and cannot be emitted to vacuum. The increase of the graphitic content directly reduces the escape depth of the internal secondary electrons and, therefore, the secondary electron yield. While being supported by the presented experimental findings, this interpretation is rather simplified. Indeed, the SEY_{max} of pure graphite is 1.3 [40], suggesting that imperfections of the graphitic phase in a-C might contribute to its low SEY.

Although the presence of hydrogen and deuterium in the thin films is not directly responsible for the SEY increase, it plays a key role in reducing the graphitic amount. Indeed, the H/D incorporation will naturally reduce the relative contents of both graphitic and diamond-like phases in a-C:H(D). It was revealed in our previous work that incorporation of deuterium is a consequence of target poisoning, yielding in the sputtering of CD and CD_2 molecules in parallel with C atoms [15]. At the same time, pure carbon phases can only be deposited by magnetron sputtering of C atoms. The relative amount of pure carbon phases is directly related to the flux ratio of C and CD_x particles leaving the target and travelling towards the substrate. In the case of the sample 10D, this ratio was very low due to the strong target poisoning, resulting in a polymer-like film.

4. Materials and Methods

All details of the thin film deposition procedure are explained in [15]. Briefly, the films were deposited by magnetron sputtering from a 50 mm diameter graphite target. The total operating pressure was set to 2 Pa, consisting of Ar and small quantities of D_2, to study deuterium incorporation into the films. The substrates were mounted 93 mm away from the graphite target and the discharge power fixed at 30 W. Five sets of samples were deposited on Si single crystal and quartz substrates for different characterisations: the reference (without D_2 added to the discharge gas), 0.2D (0.2 vol% of added D_2), 0.5D (0.5 vol% of D_2), 1D (1.3 vol% of D_2) and 10D (10.9 vol% of D_2). D_2 was added to distinguish the deliberately introduced contaminants from hydrogen contamination from the residual gas. The system was baked prior to each run for 24 h at 230 °C to minimise the natural contamination, keeping the residual gas pressure in the low 10^{-6} Pa range or better (N_2 equivalent). A new graphite target was used for each run. The deposition rate was 10–15 nm/h, generally increasing for higher D_2 partial pressure, p_{D2}. The thin film thicknesses ranged between 486 and 719 nm (measured using cross-sectional SEM). The samples were transferred to different laboratories in stainless steel vacuum chambers, pre-evacuated using a turbomolecular pump and filled with N_2 gas.

UPS and XPS measurements of 'as-received' samples were performed on an AXIS SUPRA setup (Kratos Analytical), containing both UV and monochromatic X-ray sources. XPS measurements were performed using the monochromated Al Kα line (photon energy of 1486.7 eV), and a spectrometer pass energy of 80 eV (survey spectra) and 5 eV (high resolution spectra). UPS measurements were performed by means of the He I α line (photon energy of 21.22 eV) and the spectrometer pass energy of 5 eV. The binding energy scale for the UPS and XPS measurements were both calibrated using a sputter-cleaned Ag sample, based on the position of the Ag $3d_{5/2}$ line and of the top of the valence band. Fitting of graphitic contributions was based on the XPS measurements of freshly cleaved Highly Oriented Pyrolytic Graphite (HOPG). A correction of the raw UPS spectra was made by removing the contributions of the He I β line (energy shift of 1.87 eV, intensity of 1.2% with respect to the He I α line). All samples were conductive, apart from the sample 10D, which was measured with charge compensation using an electron flood gun.

Raman spectroscopy measurements were carried out at room temperature in a backscattering geometry on an alpha 300 R confocal Raman microscope (WITec) using a 532 nm Nd:YAG laser (2nd harmonic), as well as a 633 nm He-Ne laser for excitation. The laser beam with a power of 0.7 mW was focused on the sample using a ×50 lens (Zeiss), providing a spot with a diameter of about 1 μm. The spectra were collected with a 600 groove/mm grating using 5 acquisitions with 2 s acquisition time. The same setup was used to perform photoluminescence measurements with two excitation wavelengths: 532 nm and 633 nm. For each sample, the spectra were acquired on several spots to check their lateral uniformity.

FTIR measurements were performed in a vacuum in the wave number range 500–5000 cm^{-1}, using a Vertex 80v system (Bruker) in conventional reflection and transmission mode, as well as in the attenuated total reflection (ATR) configuration using a Ge crystal.

HREELS measurements were performed in a UHV system (operating pressure in the 10^{-7} Pa range) using a LK Technologies 2000R spectrometer. Further details on this experimental setup are provided in Appendix A, together with the experimental results.

5. Conclusions

Amorphous carbon coatings, deliberately modified through the incorporation of deuterium during magnetron sputtering deposition, were thoroughly analysed using different electron and vibrational spectroscopies. Adding deuterium enabled us to differentiate its contribution from that of hydrogen—the latter being present as a natural contaminant from the residual gas during the deposition. These data were combined with previous composition and optical measurements [15] to reveal the role of H/D incorporation in the change of the secondary electron emission characteristics.

The vibrational spectroscopies demonstrated that the majority of the deuterium is bonded with sp^2 carbon, while the surface hydrogen is mainly present in the form saturated hydrocarbons. Both XPS and UPS (in combination with the Tauc gap) measurements revealed the non-uniform character of the samples, which is common for a–C materials [16]. A peak model was established, enabling us to determine the relative amount of carbon in the graphitic phase and to correlate this quantity with the SEY and the Tauc gap. The increase of the deuterium amount in the films is accompanied by a decrease of the fraction of the graphitic component and the cluster size. Based on the results, we conclude that the high content of graphitic phases in the films is responsible for the low secondary electron emission, in the same manner as it is for a low Tauc gap [18]. A model was developed to predict the SEY of non-uniform samples, which successfully describes the obtained experimental results.

The formation of pure carbon phases (graphitic or diamond like) and hydrocarbon regions are competing processes. In our experiments, the latter was the result of target contamination by D atoms formed in the plasma, followed by the physical sputtering of CD_x molecules, representing the building blocks of hydrocarbon phases [15]. Therefore, the flux ratio of the CD_x and C particles approaching the substrate was detrimental in this case for the relative graphitic content in the films.

The clusters of graphitic phases within the films have a local energy gap, close to 0 eV, which reduces the escape depth of electrons travelling through it and, consequently, also reduces the secondary electron yield.

Supplementary Materials: The supporting information can be downloaded at: https://www.mdpi.com/article/10.3390/ijms241612999/s1.

Author Contributions: Conceptualisation, N.B. and P.C.P.; methodology, N.B and P.C.P.; software, N.B.; validation, A.M.F., M.H. and M.V.; formal analysis, N.B., J.D., M.F.C. and A.M.M.B.d.R.; investigation, C.F.A., J.D., M.F.C., A.M.M.B.d.R., N.P.B., Y.D., H.N. and M.R.; writing—original draft preparation, N.B. and P.C.P.; writing—review and editing, M.H., O.M.N.D.T., C.F.A. and A.M.M.B.d.R.; visualisation, C.F.A.; supervision, M.V., I.M.M.F. and E.A. All authors have read and agreed to the published version of the manuscript.

Funding: This research was funded by the Portuguese Foundation for Science and Technology (FCT) in the frame of the project CERN/FIS-TEC/0039/2019. The support of the FCT via the grants UIDB/00068/2020, UIDP/00068/2020, UIDB/04565/2020, UIDP/04565/2020 and LA/P/0140/2020 is also gratefully acknowledged. A.M. F. wishes to thank Instituto Superior Técnico for the Scientific Employment contract IST-ID/131/2018.

Data Availability Statement: Not applicable.

Acknowledgments: We acknowledge Mauro Taborelli, from CERN, for discussions and suggestions during the work on the manuscript.

Conflicts of Interest: The authors declare no conflict of interest.

Appendix A. HREELS Measurements

Appendix A.1. Experimental Setup

HREELS measurements were performed in a UHV system (operating pressure in the 10^{-7} Pa range) using a LK Technologies 2000R spectrometer. The incidence and analysis angles, measured relative to the surface normal, were 60° and 30°, respectively. Such a geometry secures very high surface sensitivity. The analysis of the sample 1D was performed, as it was the one with potentially the highest deuterium content that can be measured (it appeared that the sample 10D was charging, as explained below). The nominal primary electron energy was 3 eV (with the elastic peak Full Width at Half Maximum (FWHM) of 12 meV). The cut-off of the spectra was measured at about 3.8 eV, corresponding to the true primary electron energy. The spectra were acquired with an energy step of 0.916 meV (7.38 cm^{-1}).

Appendix A.2. Results

In a HREELS experiment, a monoenergetic electron beam interacts with the surface region in different ways, exciting vibrational modes [41] and electronic states [42]. For non-specular conditions (different incident and analysis angles), the dominant excitation mechanism is via impact (short range) interactions, occurring at distances below 1 nm. In this regime, the technique is mainly sensitive to the molecular groups in the first atomic layer, providing information on both vibrational [43] and electronic [44] excitations.

Figure A1 displays the spectrum of the sample 1D in the vibrational energy loss range. The elastic peak is asymmetric due to the excitation of low energy phonons. From 600 to ~2000 cm^{-1}, a complex, not resolvable structure exists due to IR active modes corresponding to deformation vibrations of C-D and C-H bonds, as well as to the Raman modes, which can also be excited in the non-specular geometry [45]. In the stretching modes region, C-D (2000 to 2450 cm^{-1} range) and C-H (2750 to 3200 cm^{-1} range) vibrations are detected [46]. Even with some uncertainty of the background, each of those two structures can be fitted using two components. The first set at 2279 and 2150 cm^{-1} can be assigned to the stretching vibrations of D bonded to sp^2 and sp^3 carbon, respectively. This result is well correlated with the similar structures observed in the FTIR measurements of the sample 10D (Supplementary Information S2). Indeed, perdeuterated benzene exhibits an IR peak at 2286 cm^{-1} [47]. In addition, in our previous work dealing with selectively deuterated polystyrenes, peaks at those frequencies were also found [48]. The equivalent C–H structure can be fitted to two components at 3054 and 2938 cm^{-1}, which can be assigned to hydrogen bonded with sp^2 and sp^3 hybridised carbon, respectively. At a higher energy loss (3558 cm^{-1}), another peak is detected, which we assign to the O-H stretching in an alcohol group. The equivalent deuterated group (O-D vibration), which should be present between the C-D and C-H structures, was not detected. One possible reason is that the corresponding energy loss cross section of O-D is lower than that of O-H, similarly to the trend when comparing C-D and C-H bonds (Supplementary Information S2). In addition, the lack of this bond very likely implies that OH groups mainly originate from the surface contamination due to air exposure that took place after the deposition. This interpretation is supported by the fact that the vacuum system was baked prior to the deposition and had very low residual gas pressure (below $1 \cdot 10^{-8}$ Pa), and that the oxygen amount measured by using XPS was higher than that obtained by IBA [15].

The ratio of the surface concentrations of D (n_D) and H (n_H) atoms can be estimated from the ratios of the respective peak areas A_D and A_H, and the inelastic loss cross-sections attributed to the C-D (σ_D) and C-H (σ_H) bonds:

$$\frac{n_D}{n_H} = \frac{A_D}{A_H} \cdot \frac{\sigma_H}{\sigma_D} \tag{A1}$$

The corresponding cross-section ratios σ_H/σ_D in IR spectroscopy are around 1.81 (aromatic bonds) and 2.17 (aliphatic bonds), while the equivalent magnitudes are somewhat

lower in HREELS [43]. Bearing in mind the experimental difficulties in calibrating HREELS in that work, we prefer to use the cross-section ratios from the IR spectroscopy in the attempt to determine the concentration ratios n_D/n_H. As the cross-section ratios do not strongly depend on the bonding character, their average (1.99) was used, yielding n_D:n_H = 3.0. The same magnitude in the 1D sample is about two times greater when measured using IBA, most probably due to the very different information depths.

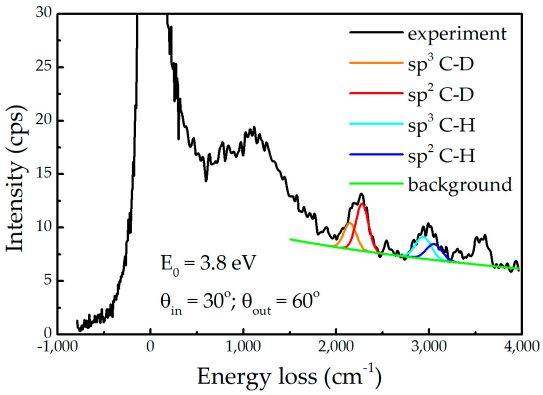

Figure A1. Vibrational HREELS spectrum of the sample 1D. The peaks obtained by fitting the C-H and C-D stretching modes are also included.

In further analysis, we consider that the cross-sections for H/D bonded with sp^2 and sp^3 carbon are approximately the same. If so, the peak intensity ratios obtained from the fits of the experimental data directly correspond to the fractions of D and H bonded with sp^2- and sp^3-hybridised carbon atoms. By implementing this approach, it appears that about 64% of the D atoms are bonded with sp^2 carbon, while this percentage is only 42% for the H atoms. One should, however, keep in mind that this ratio does not correspond directly to the relative ratios of hydrocarbon species with sp^2 and sp^3 carbon, as the relative amount of H/D in saturated aliphatic hydrocarbons is certainly higher than in compounds containing sp^2-hybridised carbon atoms.

When comparing the D:H ratio restricted to sp^2 or sp^3 carbon (using the actual intensity ratios of the corresponding cross-sections), we obtained the values of 4.23 and 2.03, respectively. While the ratio for the bonds with sp^2 carbon approaches the corresponding values obtained using IBA [15], the ratio for sp^3 carbon is clearly lower. Again, as for O-H, the results obtained can be explained by the adsorption of species that took place after the deposition, which mainly consists of aliphatic saturated hydrocarbons (airborne). Namely this is the reason for the reduced n_D:n_H ratio at the surface compared to the values measured using IBA, but also for the different ratios in the case of the sp^2 and sp^3 carbon hybridisations.

Appendix B. Modelling SEY from Non-Uniform A-Carbon Samples

Appendix B.1. Semi-Empirical Theory of Secondary Electron Emission and Its Application to Graphitic and Polymeric Samples

The semi-empirical theory of secondary electron emission is based on the following assumptions [49]:

- all primary electrons have the same range R in a material, which can be described by the power law $R = b \cdot E^n$, with E being the energy of incident electrons, while b is the material constant;
- the number of internal secondary electrons generated in the depth interval $(z, z + \Delta z)$ is directly proportional to the stopping power of primary electrons $S(z) = -dE/dz$, $\Delta N(z) = S(z)\Delta z/\varepsilon$, where ε is the effective energy required to create one internal secondary electron;

- the electron stopping power is assumed to be constant, and its average value along the trajectory $E/R(E)$ is frequently used;
- the probability that an internal secondary electron will be emitted is $0.5 \cdot \exp(-z/\lambda)$, where λ is an electron escape depth (a material dependent parameter).

Starting from these assumptions, one can easily derive the following equation for the energy dependence of SEY:

$$\mathrm{SEY} = \frac{0.5 \cdot \lambda}{\varepsilon \cdot \mathrm{b}} \cdot \frac{1 - \mathrm{e}^{-\frac{\mathrm{b} \cdot \mathrm{E}^{\mathrm{n}}}{\lambda}}}{\mathrm{E}^{\mathrm{n}-1}} \tag{A2}$$

After introducing the relative energy $E_r = E/E_m$, where E_m is the energy at which SEY has maximum, and a parameter $x = R(E_m)/\lambda$, the expression (A2) can be transformed into:

$$\mathrm{SEY_r} = \frac{\mathrm{SEY}}{\mathrm{SEY_{max}}} = \frac{1}{1 - \mathrm{e}^{-\mathrm{x}}} \cdot \frac{1 - \mathrm{e}^{-\mathrm{x} \cdot \mathrm{E_r}^{\mathrm{n}}}}{\mathrm{E_r}^{\mathrm{n}-1}} \tag{A3}$$

As x is the solution of the transcendent equation $\mathrm{e}^{\mathrm{x}} = 1 + \frac{\mathrm{n}}{\mathrm{n}-1} \cdot \mathrm{x}$ [50], the shape of the $SEY(E)$ curve is fully described by the single parameter n, which can then be obtained by fitting the experimental $SEY(E)$ curve to eq. B2 [40]. By combining Equations (A2) and (A3), the knowledge of n enables us to calculate the energy ε as:

$$\varepsilon = \frac{0.5 \cdot (1 - \mathrm{e}^{-\mathrm{x}}) \cdot \mathrm{E_m}}{\mathrm{x} \cdot \mathrm{SEY_{max}}} \tag{A4}$$

In our approach, we consider the reference sample (without D incorporation) and the 10D sample as representatives of dominantly graphitic and polymeric samples, respectively. Their $SEY_r(E_r)$ curves (obtained from the $SEY(E)$ curves from [15]), presented in Figure A2, can be well described within the semi-empirical theory using the values n = 1.6 (reference sample) and n = 1.5 (10D sample). The corresponding parameters x were then calculated by solving the above mentioned transcendent equation, as well as the effective energies ε using eq. B3 and the experimental values for E_m and SEY_{max}. The obtained values for the reference sample and the 10D sample are 60.4 and 40.8 eV, respectively. The escape depths used for graphitic and organic carbon samples, taken from [11], are 4.9 and 11 nm, respectively. After calculating the factors b as $x \cdot \lambda / {E_m}^n$ (from the assumed $R(E)$ dependence and the definition of the parameter x), we were able to calculate the SEY curves in the framework of the semi-empirical theory.

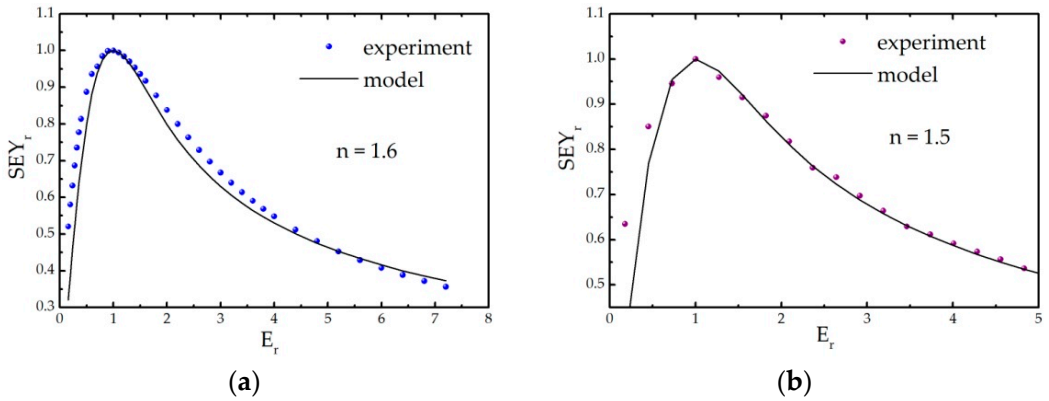

(**a**) (**b**)

Figure A2. Determination of the parameter n in the case of the (**a**) the reference sample (without D) and (**b**) the 10D sample, representing dominantly graphitic and polymeric samples, respectively.

The experimental and modelled SEY curves are compared in Figure A3. Although the experimental data were used to derive some of the model parameters, namely n and ε, it should be stressed that there were no adjustments of the calculated values to the experimental SEY curves. With this in mind, the semi-empirical theory provides a very good description of the experimental SEY curves. This is particularly valid for the reference

sample (Figure A3a), for which an excellent agreement for both SEY_{max} and E_m is obtained. That is not the case with the polymeric sample, particularly concerning the maximum position. A possible reason for this discrepancy could be the different measurement method that was used for the sample 10D due to its low conductivity (see Section 2 for details). Nevertheless, even for that sample, the model curve appears to be a relatively good representative of the experimental dependence.

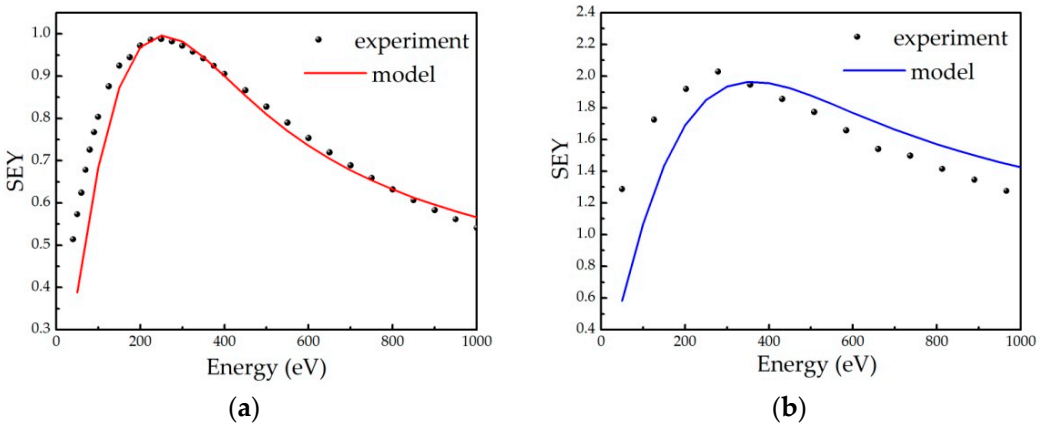

Figure A3. Comparison of the experimental and calculated SEY in the case of the (**a**) reference and (**b**) 10D sample.

Appendix B.2. Model Description

The semi-empirical theory, including its recent upgrade for multilayer systems [38], is a 1D continuous model. Therefore, a non-uniform material can be only considered as a multilayer system. For a fixed sample composition, there is a huge number of depth distributions of polymeric and graphitic layers (here designated as configurations) with very different SEYs. Some of the possible configurations in the case of a sample consisting of 30% of graphitic component are presented in Figure A4. Extreme configurations, consisting of only two layers (one for each component), would have very different SEYs, depending on which phase is on the top. As a representative configuration cannot be determined, we considered this problem within a Monte Carlo simulation approach.

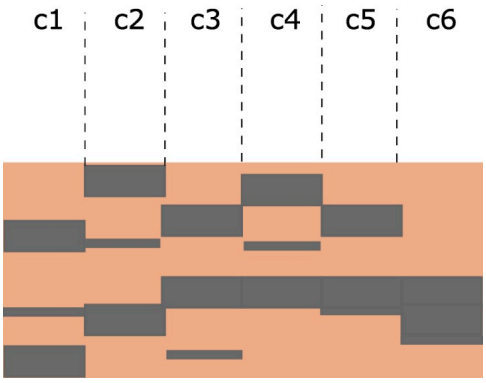

Figure A4. Illustration of different configurations *ck* ($k = 1, 2...$), each containing the same relative amounts of graphitic (grey) and polymeric (brown) regions, which will be characterised with very different SEY curves.

The first step was to determine the range of the primary electrons using the assumptions built into the semi-empirical theory: the stopping power of electrons in each region i is constant and can be determined as $S_i = E/R_i$, where R_i is the range in a uniform sample consisting of the component i. Let L_p and L_g be the total lengths of the trajectories of

primary electrons passing through the polymeric and graphitic regions, respectively. The range of primary electrons will then be $R = L_p + L_g$. As all of the primary electron energy is transferred to the material after the primary electrons pass the trajectory of length R, we can write $E = S_g \cdot L_g + S_p \cdot L_p = \frac{E}{R_g} \cdot L_g + \frac{E}{R_p} \cdot L_p$, i.e., $1 = \frac{L_g}{R_g} + \frac{L_p}{R_p}$. We assume that the fraction of trajectories that pass through the component i equals the relative concentration of that component n_i i.e., $L_i/R = n_i$. In that case, the range of primary electrons through the two-component sample can be written as:

$$R = \left(\frac{n_p}{R_p} + \frac{n_g}{R_g} \right)^{-1} \tag{A5}$$

The sample is considered to have a thickness equal to the range R obtained for the maximum primary electron energy, calculated from the known composition, using eq. B4. The sample is divided into 100 layers of equal thickness, $\Delta z = R/100$. The composition of each layer is varied within the Monte Carlo approach, knowing that the probability that a particular layer is graphitic/polymeric equals $n_g/(1 - n_g)$. Once a configuration is formed, the SEY is calculated by creating in each layer of index i exactly $S_i \cdot \Delta z/\varepsilon_i$ internal secondary electrons, which will leave the material with a probability of $0.5 \cdot \prod_{j=1}^{i-1} e^{-\frac{\Delta z}{\lambda_j}}$ (the indices i and j increase with the layer depth). For a particular configuration, the SEY is calculated for different primary electron energies. This procedure is then repeated for M different configurations characterised by the same sample composition, and the final $SEY(E)$ is obtained as an average of all the curves obtained for different configurations. The results presented in the paper are obtained for $M = 1000$.

References

1. Gröbner, O. Bunch induced multipactoring. In Proceedings of the 10th International Conference on High-Energy Accelerators, Serpukhov, Russia, 11–17 July 1977; CM-P0064850; CERN Libraries: Geneva, Switzerland, 1977.
2. Cimino, R.; Collins, I.R.; Furman, M.A.; Pivi, M.; Ruggiero, F.; Rumolo, G.; Zimmermann, F. Can low-energy electrons affect high-energy physics accelerators? *Phys. Rev. Lett.* **2004**, *93*, 014801. [CrossRef]
3. Kishek, R.A.; Lau, Y.Y.; Ang, L.K.; Valfells, A.; Gilgenbach, R.M. Multipactor discharge on metals and dielectrics: Historical review and recent theories. *Phys. Plasmas* **1998**, *5*, 2120–2126. [CrossRef]
4. Puech, J.; Lapierre, L.; Sombrin, J.; Semenov, V.; Sazontov, A.; Buyanova, M.; Vdovicheva, N.; Jordan, U.; Udiljak, R.; Anderson, D.; et al. A multipactor threshold in waveguides: Theory and experiment. In *Quasi-Optical Control of Intense Microwave Transmission*; NATO Science Series II: Mathematics, Physics, and Chemistry; Hirshfield, J.L., Petelin, M.I., Eds.; Springer: Dordrecht, The Netherlands, 2006; Volume 203.
5. Hillairet, J.; Goniche, M.; Fil, N.; Belhaj, M.; Puech, J. Multipactor in High Power Radio-Frequency Systems for Nuclear Fusion. In Proceedings of the International Workshop on Multipactor, Corona and Passive Intermodulation, MULCOPIM 2017, Noordwijk, The Netherlands, 5–7 April 2017.
6. Skripka, G.; Iadarola, G.; Mether, L.; Rumolo, G. Non-monotonic dependence of heat loads induced by electron cloud on bunch population at the LHC. *Eur. Phys. J. Plus* **2022**, *137*, 849. [CrossRef]
7. Vallgren, C.Y.; Arduini, G.; Bauche, J.; Calatroni, S.; Chiggiato, P.; Cornelis, K.; Pinto, P.C.; Henrist, B.; Métral, E.; Neupert, H.; et al. Amorphous carbon coatings for the mitigation of electron cloud in the CERN super proton synchrotron. *Phys. Rev. Spec. Top.-Accel. Beams* **2011**, *14*, 071001. [CrossRef]
8. Willeke, F.; Beebe-Wang, J. *Electron Ion Collider Conceptual Design Report 2021*; Brookhaven National Lab.: Upton, NY, USA; Thomas Jefferson National Accelerator Facility (TJNAF): Newport News, VA, USA, 2021. [CrossRef]
9. Verdu-Andres, S.; Verdu-Andres, S.; Brennan, J.M.; Blaskiewicz, M.; Gu, X.; Gupta, A.; Hershcovitch, A.; Mapes, M.; McIntyre, G.; Muratore, J.; et al. A beam screen to prepare the RHIC vacuum chamber for EIC hadron beams: Conceptual design and requirements. In Proceedings of the 12th International Particle Accelerator Conference—IPAC'21, Campinas, Brazil, 24–28 May 2021. Available online: https://www.osti.gov/servlets/purl/1784486 (accessed on 1 July 2023).
10. Egerton, R.F. Electron-Energy Loss Spectroscopy in the Electron Microscope, 3rd ed.Springer: New York, NY, USA, 2011.
11. Ono, S.; Kanaya, K. The energy dependence of secondary emission based on the range-energy retardation power formula. *J. Phys. D Appl. Phys.* **1979**, *12*, 619. [CrossRef]
12. Pinto, P.C.; Calatroni, S.; Chiggiato, P.; Edwards, P.; Mensi, M.; Neupert, H.; Taborelli, M.; Yin-Vallgren, C. Carbon coating of the SPS dipole chambers. Proceedings of ECLOUD'12, La Biodola, Isola d'Elba, Italy, 5–9 June 2012; pp. 141–148.
13. Santos, A.; Bundaleski, N.; Shaw, B.J.; Silva, A.G.; Teodoro, O.M.N.D. Increase of Secondary Electron Yield of Amorphous Carbon Coatings under High Vacuum Conditions. *Vacuum* **2013**, *98*, 37–40. [CrossRef]

14. Fernández, H.M.; Himmerlich, M.; Pinto, P.C.; Coroa, J.; Sousa, D.; Baris, A.; Taborelli, M. The impact of H2 and N2 on the material properties and secondary electron yield of sputtered amorphous carbon films for anti-multipacting applications. *Appl. Surf. Sci.* **2021**, *542*, 148552. [CrossRef]
15. Adame, C.F.; Alves, E.; Barradas, N.P.; Pinto, P.C.; Delaup, Y.; Ferreira, I.M.M.; Neupert, H.; Himmerlich, M.; Pfeiffer, S.; Rimoldi, M.; et al. Amorphous carbon thin films: Mechanisms of hydrogen incorporation during magnetron sputtering and consequences for the secondary electron emission. *J. Vac. Sci. Technol. A* **2023**, *41*, 043412. [CrossRef]
16. Ferrari, A.C.; Robertson, J. Interpretation of Raman spectra of disordered and amorphous carbon. *Phys. Rev. B* **2000**, *61*, 14095. [CrossRef]
17. Roy, D.; Samub, G.F.; Hossain, M.K.; Janáky, C.; Rajeshwar, K. On the measured optical bandgap values of inorganic oxide semiconductors for solar fuels generation. *Catal. Today* **2018**, *300*, 136–144. [CrossRef]
18. Robertson, J. Diamond-like amorphous carbon. *Mater. Sci. Eng. R Rep.* **2002**, *37*, 129–281. [CrossRef]
19. Zhang, L.; Wei, X.; Wang, F. A ternary phase diagram for amorphous carbon. *Carbon* **2015**, *94*, 202–213. [CrossRef]
20. Kaciulis, S. Spectroscopy of carbon: From diamond to nitride films. *Surf. Interface Anal.* **2012**, *44*, 1155–1161. [CrossRef]
21. Mérel, P.; Tabbal, M.; Chaker, M.; Moisa, S.; Morgot, J. Direct evaluation of the sp^3 content in diamond-like-carbon films by XPS. *Appl. Surf. Sci.* **1998**, *136*, 105–110. [CrossRef]
22. Morgan, D.J. Comments on the XPS analysis of carbon materials. *C* **2021**, *7*, 51. [CrossRef]
23. Biesinger, M.C. Accessing the robustness of adventitious carbon for charge referencing (correction) purposes in XPS analysis: Insights from a multi-user facility data review. *Appl. Surf. Sci.* **2022**, *597*, 153681. [CrossRef]
24. Beamson, G.; Briggs, D. *High Resolution XPS of Organic Polymers—The Scienta ESCA300 Database*; Wiley Interscience: Hoboken, NJ, USA, 1992.
25. Fairley, N.; Fernandez, V.; Richard-Pluet, M.; Guillot-Deudon, C.; Walton, J.; Smith, E.; Flahaut, D.; Greiner, M.; Biesinger, M.; Tougaard, S.; et al. Systematic and collaborative approach to problem solving using X-ray photoelectron spectroscopy. *Appl. Surf. Sci. Adv.* **2021**, *5*, 100112. [CrossRef]
26. Scofield, J.H. Hartree-Slater subshell photoionisation cross-sections at 1254 and 1487 eV. *J. Electron Spectrosc. Relat. Phenom.* **1976**, *8*, 129–137. [CrossRef]
27. Law, A.; Johnson, M.; Hughes, H. Synchrotron-radiation-excited angle-resolved photoemission from single-crystal graphite. *Phys. Rev. B* **1986**, *34*, 4289. [CrossRef] [PubMed]
28. Ozfidan, I.; Karkusinski, M.; Hawrylak, P. Electronic properties and electron-electron interactions in graphene quantum dots. *Phys. Status Solidi RRL* **2016**, *10*, 13–23. [CrossRef]
29. Ferrari, A.C.; Robertson, J. Raman spectroscopy of amorphous, nanostructured, diamond-like carbon, and nanodiamond. *Philos. Trans. R. Soc. Lond. A* **2004**, *362*, 2477–2512. [CrossRef]
30. da Costa, M.E.H.M.; Freire, F.L., Jr. Deuterated amorphous carbon films: Film growth and properties. *Surf. Coat. Technol.* **2010**, *204*, 1993–1996. [CrossRef]
31. Ferrari, A.C.; Basko, D.M. Raman spectroscopy as a versatile tool for studying the properties of graphene. *Nat. Nanotechnol.* **2013**, *8*, 235–246. [CrossRef] [PubMed]
32. Nakahara, S.; Stauss, S.; Miyazoe, H.; Shizuno, T.; Suzuki, M.; Kataoka, H.; Sasaki, T.; Terashima, K. Pulsed Laser Ablation Synthesis of Diamond Molecules in Supercritical Fluids. *Appl. Phys. Express* **2010**, *2*, 096201. [CrossRef]
33. Rusli; Robertson, J.; Amaratunga, G.A.J. Amaratunga, Photoluminescence behavior of hydrogenated amorphous carbon. *J. Appl. Phys.* **1996**, *80*, 2998–3003. [CrossRef]
34. Merlen, A.; Buijnsters, J.G.; Pardanaud, C. A Guide to and Review of the Use of Multiwavelength Raman Spectroscopy for Characterizing Defective Aromatic Carbon Solids: From Graphene to Amorphous Carbons. *Coatings* **2017**, *7*, 153. [CrossRef]
35. Pardanaud, C.; Martin, C.; Roubin, P.; Giacometti, G.; Hopf, C.; Schwarz-Selinger, T.; Jacob, W. Raman spectroscopy investigation of the H content of heated hard amorphous layers. *Diam. Relat. Mater.* **2013**, *34*, 100–104. [CrossRef]
36. Robertson, J. Photoluminescence Mechanism in amorphous hydrogenated carbon. *Diam. Relat. Mater.* **1996**, *5*, 457–460. [CrossRef]
37. Lye, R.G.; Dekker, A.J. Theory of Secondary Emission. *Phys. Rev.* **1957**, *107*, 977–981. [CrossRef]
38. He, Y.; Shen, T.; Wang, Q.; Miao, G.; Bai, C.; Yu, B.; Yang, J.; Feng, G.; Hu, T.; Wang, X.; et al. Effect of atmospheric exposure on secondary electron yield of inert metal and its potential impact on the threshold of multipactor effect. *Appl. Surf. Sci.* **2020**, *520*, 146320. [CrossRef]
39. Lin, Y.; Joy, D.C. A new examination of secondary electron yield data. *Surf. Interface Anal.* **2005**, *37*, 895–900. [CrossRef]
40. Bundaleski, N.; Belhaj, M.; Gineste, T.; Teodoro, O.M.N.D. Calculation of the angular dependence of the total electron yield. *Vacuum* **2015**, *122*, 255–259. [CrossRef]
41. Ibach, H.; Mills, D.L. *Electron Energy Loss Spectroscopy and Surface Vibrations*; Academic Press: New York, NY, USA, 1982.
42. Botelho do Rego, A.M.; Rei Vilar, M.; Lopes da Silva, J. Mechanisms of vibrational and electronic excitations of polystyrene films in high resolution electron energy loss spectroscopy. *J. Electron Spectrosc. Relat. Phenom.* **1997**, *85*, 81–91. [CrossRef]
43. Rei Vilar, M.; Botelho do Rego, A.M.; Lopes da Silva, J.; Abel, F.; Quillet, V.; Schott, M.; Petitjean, S.; Jerome, R. Quantitative Analysis of Polymer Surfaces and Films Using Elastic Recoil Detection Analysis (ERDA), Fourier Transform Infrared Spectroscopy (FTIRS), and High-Resolution Electron Energy Loss Spectroscopy (HREELS). *Macromolecules* **1994**, *27*, 5900–5906. [CrossRef]

44. Botelho do Rego, A.M.; Ferraria, A.M.; Rei Vilar, M. Grafting of Cobaltic Protoporphyrin IX on Semiconductors toward Sensing Devices: Vibrational and Electronic High-Resolution Electron Energy Loss Spectroscopy and X-ray Photoelectron Spectroscopy Study. *J. Phys. Chem. C* **2013**, *117*, 22298–22306. [CrossRef]
45. Botelho do Rego, A.M.; da Silva, J.L.; Rei Vilar, M.; Voltz, R. Resonance mechanisms in electron energy loss spectra of stearic acid Langmuir-Blodgett monolayers revealed by isotopic effects. *J. Electron Spectrosc. Relat. Phenom.* **1998**, *87*, 221–230. [CrossRef]
46. Diem, M. *Modern Vibrational Spectroscopy and Micro-Spectroscopy*, 2nd ed.; John Wiley&Sons Ltd.: Chichester, UK, 2015.
47. National Institute of Standards and Technology. *NIST Standard Reference Database SRD Number 69*; National Institute of Standards and Technology: Gaithersburg, MD, USA. [CrossRef]
48. Rei Vilar, M.; Schott, M.; Pireaux, J.J.; Grégoire, C.; Thiry, P.A.; Caudano, R.; Lapp, A.; Botelho do Rego, A.M.; Lopes da Silva, J. Study of Polymer Film Surfaces by EELS Using Selectively Deuterated Polystyrene. *Surf. Sci.* **1987**, *189*, 927–934. [CrossRef]
49. Clerc, S.; Dennison, J.R.; Hoffmann, R.; Abbott, J. On the computation of secondary electron emission models. *IEEE Trans. Plasma Sci.* **2006**, *34*, 2219–2225. [CrossRef]
50. Dionne, G.F. Origin of secondary electron emission yield curve parameters. *J. Appl. Phys.* **1975**, *46*, 3347–3351. [CrossRef]